Formation Process of Mesostructured PtRu Nanoparticles Electrodeposited on a Microemulsion Lyotropic Liquid Crystalline Template As Revealed by *in Situ* XRD, SAXS, and XANES

Yu-Chia Liang, Yu-Wan Juan, Kueih-Tzu Lu, U-Ser Jeng,* Shin-An Chen, Wei-Tsung Chuang, Chun-Jen Su, Chin-Lung Liu, Chin-Wen Pao, Jyh-Fu Lee, Hwo-Shuenn Sheu, and Jin-Ming Chen*

National Synchrotron Radiation Research Center, Hsinchu 30076, Taiwan

Ⓢ *Supporting Information*

ABSTRACT: We investigated the formation process of mesostructured PtRu nanoparticles electrochemically reduced on a microemulsion lyotropic liquid-crystalline (MLLC) template. Nonionic surfactant decaethylene glycol monohexadecyl ether (Brij 56) and heptane (2 wt %) were used to form the MLLC template of a 2D hexagonal packing. The MLLC template was proved to be more stable than the corresponding LLC one without heptane, in the uptake of the metal precursors and the accommodation of the subsequently electroreduced PtRu nanoparticles. Structural evolution from the metallic ionic precursors to the mesomorphically ordered PtRu nanoparticles as directed by the MLLC template was traced using *in situ* small-angle X-ray scattering (SAXS), *in situ* X-ray diffraction (XRD), and X-ray absorption near-edge structure (XANES) spectra, further complementary by energy-dispersive X-ray spectroscopy (EDS), scanning electron microscopy (SEM), and field emission transmission electron microscopy (FE-TEM). Integrated results indicate an earlier and faster reduction of Pt precursors than that of Ru, upon electroreduction. Mixing aggregation of the subsequently reduced metallic atoms led to uniform PtRu nanoparticles, featuring in a Pt-rich alloy crystalline core and an amorphous Ru-rich shell. Confined by the MLLC template, growth of PtRu nanoparticles in the early stage saturated to a size of ~4.5 nm. The subsequent growth was limited to the increase of number density of the nanoparticles. In the late stage, prolonged reduction led to highly populated nanoparticles that could further interconnect into an inverted mesostructure of the hexagonal packed MLLC template. The proposed MLLC template and the elucidated global and local structural evolution provide insights and implications on the growth mechanism and morphological control strategies for optimum syntheses of similarly mesostructured bimetallic nanoparticles of tailored size and degree of alloy.
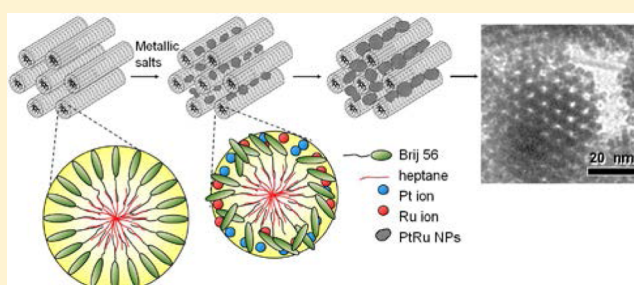
1. INTRODUCTION

Ordered mesoporous metallic materials with large specific surface areas and tailored pore sizes present considerable interests because of their many prospective applications in diverse technologies, such as metallic catalysts, fuel cells, batteries, electrochemical supercapacitors, and sensors.[1−4] Various synthetic approaches have been developed to achieve controls over the composition, structure, size, and shape of the mesoporous metallic materials.[5] Mesostructured metal or alloy materials are generally synthesized from templates of, for instance, that used in mesoporous silica materials (e.g., MCM-41, MCM-48, and SBA-15); removing the templates results in mesoporous metal frameworks of large reactive surfaces.[6,7] Among them, Pt-alloy-based porous materials were shown to exhibit an efficient performance for the electrocatalysis of the oxidation of carbon monoxide and methanol.[13−15] In particular, mesoporous PtRu alloys were recognized as promising anodic electrocatalysts for the oxidation of methanol in low-temperature polymer-membrane fuel cells.[16] In developing efficient fuel-cell electrocatalysts, surface morphology, composition,

crystalline structure, and nanostructure of the mesoporous PtRu alloys are considered as critical factors.[17−19] However, most mesoporous metal materials deposited on flat gold or platinum foil substrates from direct physical casting, chemical, or electrochemical reduction exhibited relatively less nanostructural features, namely, less surface area.[20−22] A substantial improvement in catalytic efficiency would be expected when metallic nanoparticles are mesostructured with nanopores to further elevate the density of metallic surfaces.

Previously, Attard et al. reported a unique synthesis for mesoporous platinum films from a planar electrode via lyotropic liquid-crystal (LLC) templates of nonionic surfactants.[8,23−25] This approach opened an attractive route in preparing mesoporous metal or alloy materials, such as, Pd, Ni, Pt, ferromagnetic, or PtRu alloy.[9−12] Nevertheless, high loading of metal precursors and/or accommodation of the reduced
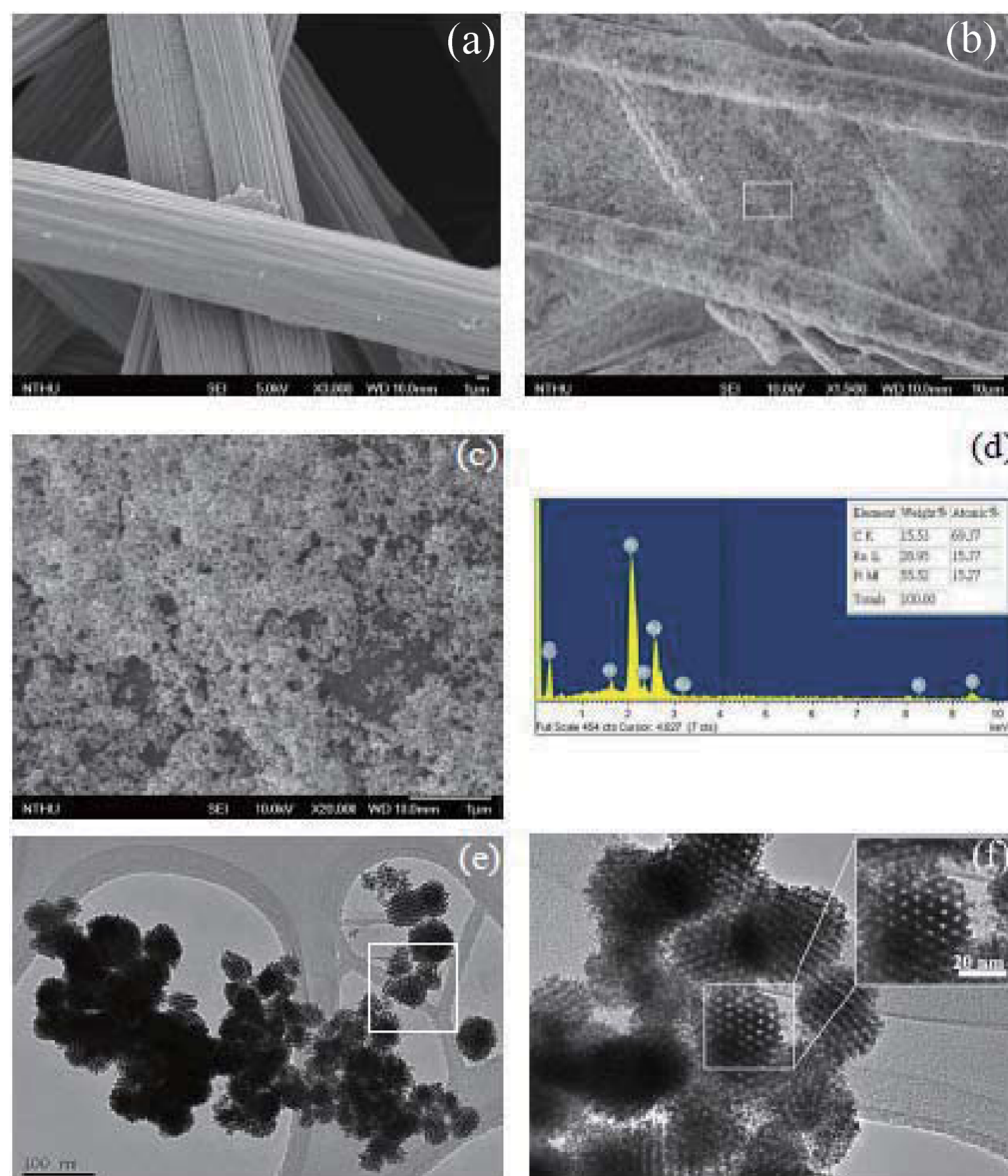
Figure 1. (a) FE-SEM image of carbon fiber paper with randomly distributed graphite fibers of diameter ~10 μm. (b) Low-magnified FE-SEM image of carbon fiber paper after electrodeposition (c) Highly magnified FE-SEM image of the square area of (b). (d) EDS pattern of m-PtRu NP. (e) Low-magnified TEM image of m-PtRu NP. (f) Highly magnified TEM image of m-PtRu NP. Inset shows a zoom-in view for the hexagonally packed nanopores embedded in the mesostructured m-PtRu.

highly populated nanoparticles therein deteriorated substantially the ordering of the LLC template, leading to smaller sizes of the mesostructured frameworks or reduced metal surface density. In a similar synthesis application, microemulsion type of LLC (MLLC) templates containing small alkane molecules of a selected chain length exhibited a convenient control over the nanopore sizes of the silicate mesostructures.[26] Here, we demonstrate that the MLLC type of templates can be adopted for the formation of mesostructured Pt−Ru bimetallic nanoparticles for improved template stability over an electroreduction process of the nanoparticles therein, in addition to the pore size control.

In this study, *in situ* synchrotron small-angle X-ray scattering (SAXS), *in situ* X-ray diffraction (XRD), and X-ray absorption spectroscopy (XAS) were used to trace the structural evolution of the formation of MLLC-templated Pt−Ru nanoparticles, during electroreduction. From which, structural evolution could

be traced from the metallic ionic precursors to their reduction into atoms and the subsequent mixing aggregation of the metallic atoms into PtRu nanoparticles; especially, these nanoparticles further organize into a mesostructure directed by the hexagonal packed MLLC template.[27] Complementarily, dispersive X-ray spectroscopy (EDS), scanning electron microscopy (SEM), and field emission transmission electron microscopy (FE-TEM) were used to illustrate consistent/complementary structural features.[28] The correlated local and global structural modifications observed in the formation process of the MLLC−nanoparticle complex reveal the formation mechanism and critical control parameters in the preparation of mesomorphically ordered bimetallic nanoparticles. Especially, the proposed MLLC template demonstrates the advantages and potential morphology control in the syntheses of mesoporous alloy materials with high density of metal surfaces.

2. EXPERIMENTAL PROCEDURES

2.1. Chemicals, Precursor Preparation, and Electrodeposition. The surfactant decaethylene glycol monohexadecyl ether (Brij 56, 98%, Fluka), dihydrogen hexachloroplatinate(IV) hydrate ($H_2PtCl_6 \cdot 6H_2O$, 99.9%, Aldrich), ruthenium trichloride ($RuCl_3 \cdot xH_2O$), and heptane (Sigma-Aldrich) were used as received. Gelatinous precursor solutions comprising Brij 56 (2.19 g), H_2PtCl_6 (1.0 g), $RuCl_3$ (0.51 g), deionized water (1.51 g), and heptane (0.106 g) at room temperature were prepared. The mixture was stirred vigorously under a heating cycle between ambient temperature and 80 °C until a homogeneous mixture was reached. The mixture was filled in a three-electrode cell consisting of a Pt plate, a reference microelectrode (with saturated Ag/AgCl), and a carbon paper substrate. With a constant potential (−0.15 V vs Ag/AgCl), PtRu nanoparticles were electrodeposited on the MLLC template. After electroreduction, the product was immersed alternatively in ethanol and deionized water several times to remove residual species.

2.2. Measurements. SEM images were measured at 15 kV with a JEOL JSM-7000F microscope, equipped with an accessory for energy-dispersive X-ray spectroscopy (EDS) (Inca, Oxford Instruments). TEM images were obtained by a JEOL JEM-2100 microscope with 200 kV; samples were mounted on a 200-mesh copper grid with lacey carbon films.

In situ XRD measurements were performed respectively at BL01C2 beamline of the National Synchrotron Radiation Research Center (NSRRC), with an 18.0 keV (wavelength λ = 0.6888 Å) beam; data collected with a Mar345 image plate were calibrated by the diffractions from mixed powders of silicon and silver behenate. For comparison, the XRD patterns were converted to Cu Kα radiation. SAXS measurements were conduced at the 23A SWAXS endstation of NSRRC, using an area detector MAR165 CCD. With a 10.0 keV (λ = 1.240 Å) beam and a sample-to-detector distance of 1830 mm, the scattering wavevector $q = 4\pi\lambda^{-1} \sin\theta$ (defined by the scattering angle θ and λ) was calibrated with a standard sample of silver behenate; the data were corrected for incoming flux, sample thickness, and electronic noise of the detector, as detailed in a previous report.[29]

X-ray absorption spectra at the Pt and Ru L-edges were measured for the MLLC-templated PtRu nanoparticles at beamlines BL01C1 and BL16A of NSRRC, respectively, with X-ray energy resolution $\Delta E/E \sim 2 \times 10^{-4}$. The Ru L-edge and Pt L-edge absorption spectra were measured in a fluorescence mode (with a Lyttle detector); X-ray energy was calibrated by the L-edge absorption of Ru powder or Pt foil. Mesostructured PtRu nanoparticles deposited at carbon fiber substrates produced with varied duration of electroreduction were washed several times with ethanol to remove the MLLC template and residual species before X-ray absorption measurements. To have a reasonable data statistics, X-ray absorption near-edge structure (XANES) spectrum was collected only after 240 s electroreduction time covering an energy range of 100 eV near the Pt or Ru L-edge. X-ray absorption spectra with extended energy range were collected for the matured PtRu nanoparticles in the final synthesis stage; data analysis for extended X-ray absorption fine structure (EXAFS) was completed using the UWXAFS package.[30]

3. RESULTS AND DISCUSSION

3.1. SEM/TEM/EDS. Figures 1a and 1b show the FE-SEM images for the clean surfaces of the substrate of carbon fiber paper before and after the electroreduction. The highly populated fine grains demonstrate that the abundant fiber surfaces of the carbon paper substrate have a potential to accept higher dosages of electrodeposition than a general flat substrate, such as an Au substrate. Figure 1c is a highly magnified FE-SEM image for the selected area in Figure 1b, exhibiting rich granule features. The compositions of the granules were further characterized with energy-dispersive X-ray spectroscopy (EDS), as shown in Figure 1d. From which, Pt:Ru atomic ratio for the granules was determined to be 49.8:50.2, suggesting strongly that the granules are composed of binary PtRu NPs. Bright-field TEM images shown in Figures 1e and 1f further illustrate that these PtRu granules (m-PtRu) are mesostructured with a hexagonal packing. As shown in a low-magnified TEM image of Figure 1e, m-PtRu exhibits a porous structure consisting of cylindrical channel pores in a 2D hexagonal packing (HEX); from the especially clearly evidenced HEX structure in Figure 1f, the HEX lattice ~7 nm can be estimated from the pore-to-pore distance. The TEM images demonstrate that a hexagonal mesoporous arrangement of PtRu framework was successfully achieved with the MLLC template.

3.2. *In Situ* XRD and SAXS. Figure 2 shows the time-resolved XRD patterns before (t = 0 s) and during the
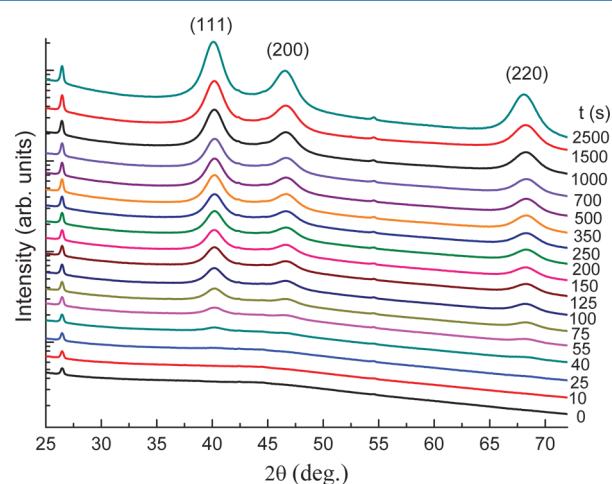

Figure 2. *In situ* time-resolved XRD patterns before (t = 0 s) and during the electrodeposition.

electrodeposition. Discernible diffractions at 2θ = 40.2°, 46.6°, and 68.2° emerged after 40 s of electroreduction, corresponding to (111), (200), and (220) reflections of a face-centered cubic (fcc) crystal structure of binary PtRu nanoparticles (NPs).[14] The intensities of these diffractions increased monotonically as the electroreduction proceeded. No characteristic reflections of pure Ru or RuO crystalline reflections could be observed; moreover, the (111), (200), and (220) reflections shifted slightly to higher angles from that for pure platinum crystallites. These together indicate that the TEM observed m-PtRu granules are composed of largely PtRu alloy nanoparticles, having an average lattice parameter a_{PtRu} = 3.884 Å deduced on the basis of d_{111} = 2.241 Å and d_{220} = 1.372 Å. This lattice value matches closely with 3.880 Å observed previously for chemically synthesized alloy $Pt_{50}Ru_{50}$.[31]

The lattice constant a_{PtRu} of the m-PtRu shifts from $a_{Pt} = 3.924$ Å of pure Pt crystals.[32] According to Vegard's law in the case of PtRu alloy[14]

$$a_{PtRu} = a_{Pt} - 0.124\chi_{Ru} \qquad (1)$$

we could extract an Ru atomic fraction $\chi_{Ru} = 0.32$ for m-PtRu. This would imply Pt-rich crystalline alloy. The previous EDS, however, revealed an equal Pt–Ru composition for the MLLC-templated PtRu granules. The XRD and EDS results may be rationalized with amorphous Ru covering the Pt-rich alloy m-PtRu nanoparticles, as supported by the XANES and EXAFS results detailed below.

We estimate the alloy degree of Ru, Ru_{al}, based on the expression

$$Ru_{al} = \chi_{Ru}/[(1 - \chi_{Ru})(Ru/Pt)_{nom}] \qquad (2)$$

in which $(Ru/Pt)_{nom}$ is the observed molar ratio (~1:1) with EDS. The $Ru_{al} = 48$ at. % thus obtained (for 1500 s reaction).[31] As we did not observed crystalline reflections of Ru or RuO crystals, the amorphous Ru (52 at. %) should be either dispersed in the matrix or coated on the Pt-rich alloy core for phase-separated Pt@Ru core–shell nanoparticles.

Figure 3 shows the time-resolved SAXS patterns observed during the electrochemical reduction of the metallic salts in the
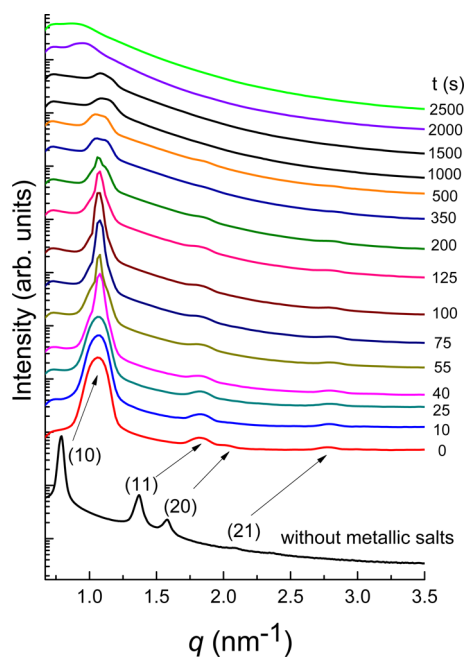
with addition of metallic salts; this might suggest that the MLLC micelles rearrange into a microemulsion structure with the headgroup region substantially disturbed with the hydrophilic chains tilted inward more, in the uptake of the metallic salts. Nonuniform intake of the metal ions could lead to polydisperse micelles, resulting in the more broadened reflections observed,[34] as compared to that for the pure LLC template (cf. the cartoon below).

After 40 s of electroreduction, a sharper peak emerged from the primary, broader peak at $q = 1.09$ nm^{-1}, and gradually enhanced toward a saturated at $t \sim 75-100$ s, indicating a much improved $p6mm$ ordering. Concomitantly, XANES result (detailed below) revealed a largely completed reduction of the metallic salts in this period time. Presumably, diminished metallic ions and expelling the reduced metallic atoms from the headgroup region resulted in more monodisperse micelles for the improved MLLC mesostructure; the corresponding ordering size estimated from the peak width is ~180 nm. Further electroreduction over 100 s led to gradually broadened $p6mm$ peaks, implying deteriorated mesostructure of the MLLC–PtRu complex. Beyond 350 s, the primary peak of $p6mm$ was significantly deteriorated and could be decomposed into two scattering humps centered respectively at $q \sim 1.05$ nm^{-1} and $q \sim 1.12$ nm^{-1}. This would suggest two types of MLLC lattices of slightly different lattice constants, of different degrees of metallic precursor electroreduction. Between 1000 and 2000 s, the $p6mm$ primary peak largely decayed and diminished to a liquid-like ordering at $q \approx 0.95$ nm^{-1}, corresponding to a mean spacing 6.6 nm of the PtRu nanoparticles. This result implies the breakout of PtRu nanoparticles from the $p6mm$ MLLC template. For prolonged electroreduction beyond 2000 s, even the liquid-like ordering peak vanishing into largely disordered PtRu nanoparticles.

3.3. XANES and EXAFS. Figure 4a shows the Pt L$_3$-edge X-ray absorption near-edge structure (XANES) spectra of the m-

Figure 3. *In situ* time-resolved SAXS patterns collected during the electrochemical reduction of the metallic salts in the MLLC template.

MLLC template. Also shown for comparison is the SAXS pattern for the LLC template without heptane and metallic salts, exhibiting relatively sharp reflections of a q-position ratio of $1:3^{1/2}:2:7^{1/2}$ of a $p6mm$ structure.[33] The corresponding lattice parameter of $p6mm$ is 8.4 nm for Brij 56 micelles with well-aligned headgroup, as extracted from the first peak position. The SAXS pattern of the MLLC with metallic salts before electroreduction (i.e., $t = 0$ s in Figure 3) revealed broad reflections with similar $p6mm$ reflections, with the peak positions notably shifted from that for the LLC without metallic salts; the corresponding lattice parameter deduced is 5.90 nm. This lattice size of MLLC is considerably reduced
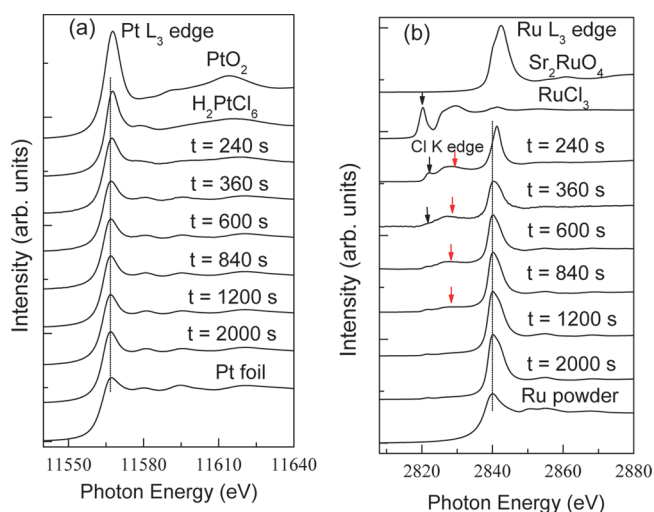

Figure 4. Evolution of the (a) Pt L$_3$-edge and (b) Ru L$_3$-dge XANES spectra of PtRu NPs produced after varied duration of electrodeposition, compared with reference spectra of Pt and Ru.

PtRu nanoparticles collected after varied duration of electrodeposition. The Pt L$_3$-edge absorption spectra of reference samples including precursor H_2PtCl_6, PtO_2 (Pt^{4+}) powder, and Pt foils are also shown for comparison. The Pt L$_3$-edge XANES spectra of the Pt precursor H_2PtCl_6 and PtO_2 exhibit a sharp

white line at $E \sim 11568$ eV, corresponding to electronic transitions from the $2p_{3/2}$ state to unoccupied 5d states near the Fermi level. The magnitude of the white line at the Pt L-edge signifies the 5d-charge depletion from the Pt site for Pt-containing samples.[35,36] Smaller intensity of the white line corresponds to a greater electron density of 5d orbitals and a lower density of Pt oxidation states. Hence, evolution of the white line intensity of the Pt L-edge can be used to monitor the progress of the Pt reduction from the oxide Pt precursors.[35,36] As illustrated in Figure 4a, the intensity of the white line of Pt L_3-edge decreased largely within the first $\sim$240 s of electro-reduction and then remained largely the same for the rest of the electroreduction. The result indicates that the reduction process of Pt^{4+} in H_2PtCl_6 was largely completed before 240 s. The later Pt L_3-edge XANES spectra of the PtRu−MLLC resemble that for a Pt foil and share nearly the same absorption rise edge. These clearly indicate that the Pt^{4+} ions in precursor H_2PtCl_6 could be reduced to metallic Pt in a short time interval. In the prolonged electroreduction with Ru atoms reduced largely, the later XANES spectra shifted gradually from that for pure Pt toward that for a PtRu alloy, indicating that the reduced Pt atoms chronically formed alloyed with the subsequently and concomitantly reduced Ru.[37]

Figure 4b shows the corresponding Ru L_3-edge XANES spectra of m-PtRu NPs produced after varied duration of electrodeposition, together with the reference spectra of the Ru precursor $RuCl_3$ (Ru^{3+}), Sr_2RuO_4 (Ru^{4+}), and metallic Ru powder for comparison. The Ru L_3-edge XANES spectrum of the RuO_2 reference exhibited an intense white line, corresponding to the electronic transitions from a $2p_{1/2}$ state to unoccupied 4d orbitals, at $E \sim 2842$ eV. As is well established previously, the pronounced pre-edge line (at $E \sim 2820$ eV) of the pre-edge feature of Cl K-edge spectra could be indicative of the highly covalent bonding of $RuCl_3$.[38] Because of the influence from Cl K-edge jump, the white line intensity of Ru L_3-edge spectra of Ru precursor $RuCl_3$ at $E \sim 2841.7$ eV was in between that of metallic Ru powder and RuO_2 reference compounds. After electroreduction for 240 s, the white-line energy of Ru L_3-edge shifted to a smaller value (by $\sim$0.5 eV), relative to that for $RuCl_3$ (Ru^{3+}). Furthermore, the pre-edge peak of the Cl K-edge XANES spectrum notably weakened and shifted to a higher E value (Figure 4b), indicating that the local environment around Ru ions was greatly altered within this short-term electroreduction. Interestingly, progressive reduction of Ru^{3+} from $RuCl_3$ could also initiate formation of Cl-containing complexes with weakly covalent bonding of Ru−Cl. The white line position of the Ru L_3-edge spectrum shifted further to a smaller E value after reaction for 360 s and remained nearly unchanged during further reaction. Especially noteworthy is that, after reaction for 360 s, the RtPu nanoparticles coexisted with intermediate RuCl-containing complexes with weakly covalent bonding of Ru−Cl because the pre-edge peak in the Cl K-edge spectrum nearly disappeared. The amounts of Cl-containing complexes decreased progressively over prolonged reaction and nearly disappeared after 840 s, as indicated by red arrows. These would imply that reduction of the Ru^{3+} ions to atoms involves intermediate. As the reduction of Ru^{3+} ions in $RuCl_3$ is already slower than that of Pt^{4+} ions in H_2PtCl_6, because the reduction potential of Ru^{3+}/Ru ($E_0 = 0.84$ V vs SHE) is less than that of Pt^{4+}/Pt ($E_0 = 1.47$ V vs SHE).[39] Formation of RuCl species further hindered the release of Ru atoms (until $\sim$600−800 s) for formation of PtRu alloy. Such two-step release of Ru atoms

for aggregation into PtRu nanoparticles may be highly relevant to the formation PtRu nanoparticles of a Pt-rich core and a Ru-rich shell, as also evidenced from the present XRD result. Parallel to the Pt case shown in Figure 4a, during the prolonged eletroreduction (after 360 s), the L_3-edge XANES spectra gradually shift toward that for the Ru powder, but maintaining a greater white line intensity than that for metallic Ru powder. This would suggest that metallic Ru atoms chronically alloyed into the earlier established Pt-rich core for the alloyed PtRu.[41]

To further support the core−shell structural feature, we have also performed EXAFS analysis for the matured m-PtRu NPs obtained after a prolonged electroreduction time of $\sim$2000 s. Figure 5 shows the radial distribution functions Fourier
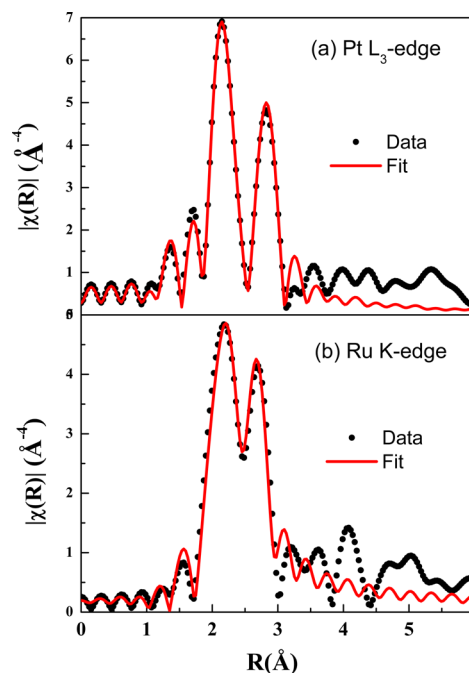

Figure 5. Radial distribution functions $\chi(R)$ of matured m-PtRu NPs Fourier transformed from the k^3-weighted EXAFS spectra respectively measured at (a) Pt L_3-edge and (b) Ru K-edge. Data were fitted with the parameters summarized in Table 1.

transformed from the k^3-weighted EXAFS spectra measured at Pt L_3-edge and Ru K-edge, respectively, which can be described by the fitted parameters summarized in Table 1; these include the coordination Pt and Ru atom numbers around a Pt atom with $N_{Pt-Pt} = 4.8$ and $N_{Pt-Ru} = 2.4$ and the coordination Ru and Pt atom numbers around a Ru atom with $N_{Ru-Pt} = 2.4$ and $N_{Ru-Ru} = 3.2$. From these coordination numbers and the Pt:Ru composition of $\approx$1:1, we have further extracted a total coordination number $N_{Pt} = 7.2$ and an extent

Table 1. Structural Parameters Derived from the EXAFS Data Analysis Shown in Figure 5 for the m-PtRu NPs, with N for the Coordination Number, R the Interatomic Distance, and σ^2 the Mean-Squared Deviation of R

	bond	N	R (Å)	σ^2 (Å^2)
Pt L_3-edge	Pt−Ru	2.4	2.71	0.0041
	Pt−Pt	4.8	2.73	0.0053
Ru K-edge	Ru−Ru	3.2	2.65	0.008 4
	Ru−Pt	2.4	2.71	0.0045

of alloying $J_{Pt} = N_{Pt-Ru}/(0.5N_{Pt}) = 0.66$ for the Pt atoms of the PtRu nanoparticles, on the basis of a previously proposed model.[42] Correspondingly $N_{Ru} = 5.6$ and $J_{Ru} = N_{Ru-Pt}/(0.5N_{Ru}) = 0.84$ are deduced for the Ru atoms. With the relative large total coordination number ($N_{Pt} = 7.2$ vs $N_{Ru} = 5.6$) and the lower extent of alloy ($J_{Pt} = 0.66$ vs $J_{Ru} = 0.84$) for the Pt atoms, the PtRu nanoparticles are consistent with Pt-rich core and Ru-rich shell, according to the structural model previously proposed for bimetal nanoparticles.[42] We note that X-ray photoelectron spectroscopy[43] or anomalous SAXS[40] may be an alternative in determining the core−shell structure.

3.4. Growth Mechanism Revealed from Integrated Structural Information. Integrated structural results can reveal more insights into the formation of the hierarchical structure comprising local bimetallic PtRu NPs and global MLLC template. The evolution of global ordering phase volume (or crystallinity) is estimated from the width of the primary reflection (10) of the *p6mm* phase of MLLC. (cf. SAXS patterns in Figure 3), whereas evolutions of the nanoparticle crystalline size and the corresponding phase volume (amounts of m-PtRu NPs) are deduced respectively from the width of the peak and integrated peak intensity of the (111) reflection (cf. XRD patterns in Figure 2). Shown in Figure 6 are the
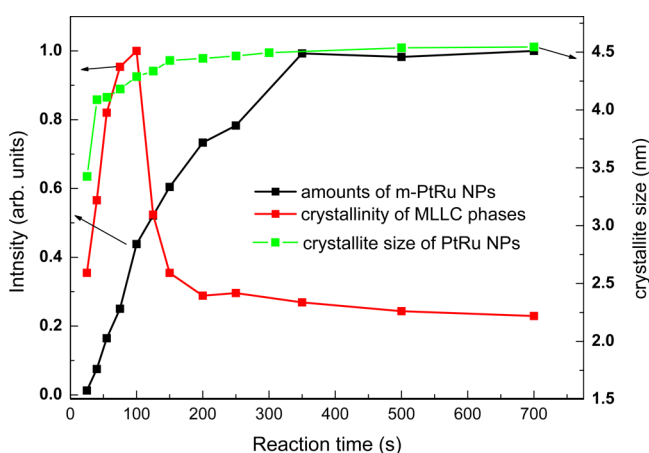

Figure 6. Crystallinity of the MLLC−PtRu complex, the amounts of m-PtRu NP, and average crystallite size of PtRu NPs as a function of electroreduction time.

correlated evolutions of the relative phase volumes of the MLLC and m-PtRu NPs and the average crystallite size of m-PtRu NPs. In view of the correlated decay and growth of the phase volumes of the MLLC and m-PtRu NPs and the saturation of particle size as illustrated in Figure 6, a plausible explanation might be proposed as the following. In the early reduction stage (∼100 s), metallic precursors were largely reduced into atoms (cf. Figure 4a) for aggregation; nucleation and growth of the PtRu nanoparticles to a roughly saturated size ∼4 nm proceeded in the MLLC confined template for ∼40% of the maxima yield of the Pr−Ru nanoparticles; this is considered as the optimum PtRu nanoparticle loading for mesostructured PtRu NPs with the currently employed MLLC template, for which an optimized ordering domain size up to ∼180 nm for the MLLC−PtRu complex was reached.

Further reduction between 100 and 350 s, the nanoparticle size grew little. Hence, the continuous increase in the phase volume of the nanoparticles (Figure 6) can be interpreted as a rapid growth in the number density of the nanoparticles of a

constant size. The mesostructure of the MLLC template was clearly influenced sensitively by continuously populating of the PtRu NPs. By the end of growth of phase volume of the nanoparticles at ∼350 s, the crystallinity of the MLLC phase is considerably deteriorated, as illustrated in Figure 6. It is likely that the slightly overgrown size (to 4.5 nm) and overpopulated nanoparticles started to break partially the confinement of the MLLC template.[44,45]

In the late stage with prolong electroreduction after 350 s, we notice that the (200) reflection (Figure 2) was slightly enhanced relative to other reflections of (111) and (220), implying a further preferred growth of the globular nanoparticles along the (200) direction for an elongated shape. As shown in Figure S1 (in Supporting Information), the PtRu NPs electrochemically reduced on the MLLC template in the later stage are also featured with an elongated shape. We believe that in this late stage of electroreduction well-developed and populated (saturated) Pt−Ru nanoparticles initiated a preferred growth and agglomeration along the template channel direction. Interconnection of these elongated PtRu NP densely populated on the MLLC template resulted in an inverted mesostructure of the hexagonally packed MLLC template. The cartoon shown in Figure 7 illustrates the structural evolution for the formation of the MLLC-directed m-PtRu nanoparticles agglomerating into a mesostructure containing hexagonally packed micelles.
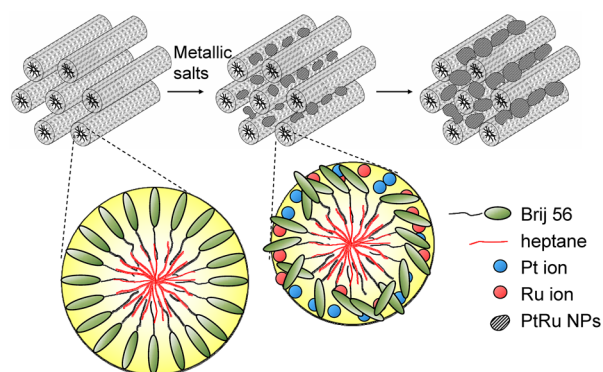

Figure 7. Scheme for forming a MLLC-directed mesoporous PtRu framework of an inverted hexagonal packing with micelles.

4. CONCLUSION

Mesostructured PtRu NPs can be successfully electrochemically reduced from their metallic salts embedded in a microemulsion type of lyotropic liquid crystalline template. With a small amount of heptane added, the MLLC template is found to have improved structural stability over the corresponding LLC template during the electroreduction. On the basis of the *in situ* SAXS/XRD and XANES, complementary with SEM, FE-TEM, and EDS results, a comprehensive structural evolution is constructed from the metallic precursors to the subsequent atom reduction, nanoparticle formation and aggregation, and the mesostructure formation. An earlier reduction of the metallic Pt precursors before that of Ru precursors should be responsible for the Pt-rich core and a Ru-rich shell structure of the alloy nanoparticles. Confined by the MLLC geometry, the nanoparticle size quickly saturates to ∼4.5 nm in an early stage of the electroreduction, which is followed by populating of the nanoparticles. In the late stage, highly populated PtRu

nanoparticles agglomerate into an inverted mesostructure of the hexagonally packed MLLC template. The integrated structural aspects and the use of the MLLC type of templates provide insights and implications in syntheses of mesostructured bimetallic nanoparticles—in tuning the nanoparticle and pore sizes by the amount of heptane included in the MLLC template and the degree of alloy by the relative reduction rates of Pt and Ru precursors.

■ ASSOCIATED CONTENT

Ⓢ Supporting Information

Figure S1. This material is available free of charge via the Internet at http://pubs.acs.org.

■ AUTHOR INFORMATION

Corresponding Author
*E-mail jmchen@nsrrc.org.tw (J.-M.C.); usjeng@nsrrc.org.tw (U.J.).
Notes
The authors declare no competing financial interest.

■ ACKNOWLEDGMENTS

■ REFERENCES

(1) (a) Huo, Q.; Margolese, D. I.; Ciela, U.; Feng, P.; Gier, T. E.; Sieger, P.; Leon, R.; Petroff, P. M.; Schuth., F.; Stücky, G. D. *Nature* **1994**, *368*, 317−321. (b) Whitehead, A. H.; Elliott, J. M.; Owen, J. R.; Attard, G. S. *Chem. Commun.* **1999**, *4*, 331−332. (c) Attard, G. S.; Corker, J. M.; Göltner, C. G.; Henke, S.; Templer, R. H. *Agnew. Chem., Int. Ed.* **1997**, *36*, 1315−1317. (d) Kulinowski, K. M.; Jiang, P.; Vaswani, H.; V. Colvin, L. *Adv. Mater.* **2000**, *12*, 833−838. (e) Xia, Y.; Gates, B.; Yin, Y.; Lu, Y. *Adv. Mater.* **2000**, *12*, 693−713.
(2) Kucernak, A.; Jiang, J. H. *Chem. Eng. J.* **2003**, *93*, 81−90.
(3) Nelson, P. A.; Elliott, J. M.; Attard, G. S.; Owen, J. R. *Chem. Mater.* **2002**, *14*, 524−529.
(4) Pell, W. G.; Conway, B. E. *J. Power Sources* **1996**, *63*, 255−266.
(5) (a) Wang, H.; Jeong, H. Y.; Imura, M.; Wang, L.; Radhakrishnan, L.; Fujita, N.; Castle, T.; Terasaki, O.; Yamauchi, Y. *J. Am. Chem. Soc.* **2011**, *133*, 14526−14529. (b) Trewyn, B. G.; Slowing, I. I.; Giri, S.; Chen, H. T.; Lin, V. S.-Y. *Acc. Chem. Res.* **2007**, *40*, 846−853. (c) Neale, N. R.; Frank, A. J. *J. Mater. Chem.* **2007**, *17*, 3216−3221. (d) Jin, H.; Wu, Q.; Chen, C.; Zhang, D.; Pang, W. *Microporous Mesoporous Mater.* **2006**, *97*, 141−144.
(6) Kresge, C. T.; Leonowicz, M. E.; Roth, W. J.; Vartuli, J. C.; Beck, J. S. *Nature* **1992**, *359*, 710−712.
(7) (a) Shin, H. J.; Ryoo, R.; Liu, Z.; Terasaki, O. *J. Am. Chem. Soc.* **2001**, *123*, 1246−1247. (b) Choi, K. S.; McFarland, E. W.; Stucky, G. D. *Adv. Mater.* **2003**, *15*, 2018−2021. (c) Guo, X. J.; Yang, C. M.; Liu, P. H.; Cheng, M. H.; Chao, K. J. *Cryst. Growth Des.* **2005**, *5*, 33−36.
(8) Attard, G. S.; Bartlett, P. N.; Coleman, N. R. B.; Elliott, J. M.; Owen, J. R.; Wang, J. H. *Science* **1997**, *278*, 838−840.
(9) Robinson, D. B.; Fares, S. J.; Ong, M. D.; Arslan, I.; Langham, M. E.; Tran, K. L.; Clift, W. M. *Int. J. Hydrogen Energy* **2009**, *34*, 5585−5591.
(10) Yamauchi, Y.; Yokoshima, T.; Mukaibo, H.; Tezuka, M.; Shigeno, T.; Momma, T.; Osaka, T.; Kuroda, K. *Chem. Lett.* **2004**, *33*, 543−543.
(11) Yamauchi, Y.; Komatsu, M.; Fuziwara, M.; Nemoto, Y.; Sato, K.; Yokoshima, T.; Sukegawa, H.; Inomata, K.; Kuroda, K. *Angew. Chem., Int. Ed.* **2009**, *48*, 7792−7797.
(12) Takai, A.; Saida, T.; Sugimoto, W.; Wang, L.; Yamauchi, Y.; Kuroda, K. *Chem. Mater.* **2009**, *21*, 3414−3423.

(13) Liu, F.; Lee, J. Y.; Zhou, W. J. *Small* **2006**, *2*, 121−128.
(14) Jiang, J. H.; Kucernak, A. *Chem. Mater.* **2004**, *16*, 1362−1367.
(15) Park, K. W.; Choi, J. H.; Kwon, B. K.; Lee, S. A.; Sung, Y. E.; Ha, H. Y.; Hong, S. A.; Kim, H.; Wieckowski, A. *J. Phys. Chem. B* **2002**, *106*, 1869−1877.
(16) Ratana, T.; Amornpitoksuk, P.; Veerasai, W. *ScienceAsia* **2006**, *32*, 253−260.
(17) Long, J. W.; Stroud, R. M.; Swider-Lyons, K. E.; Rolison, D. R. *J. Phys. Chem. B* **2000**, *104*, 9772−9776.
(18) Vogel, W.; Britz, P.; Bonnemann, H.; Rothe, J.; Hormes, J. *J. Phys. Chem. B* **1997**, *101*, 11029−11036.
(19) Takasu, Y.; Itaya, H.; Iwazaki, T.; Miyoshi, R.; Ohnuma, T.; Sugimoto, W.; Murakami, Y. *Chem. Commun.* **2001**, *4*, 341−342.
(20) Yamauchi, Y.; Kuroda, K. *Electrochem. Commun.* **2006**, *8*, 1677−1682.
(21) Yamauchi, Y.; Takai, A.; Komatsu, M.; Sawada, M.; Ohsuna, T.; Kuroda, K. *Chem. Mater.* **2008**, *20*, 1004−1011.
(22) Tominaka, S.; Hayashi, T.; Nakamura, Y.; Osaka, T. *J. Mater. Chem.* **2010**, *20*, 7175−7182.
(23) Armatas, G. S.; Kanatzidis, M. G. *Science* **2006**, *313*, 817−820.
(24) Bartlett, P. N.; Birkin, P. N.; Ghanem, M. A.; de Groot, P.; Sawicki, M. *J. Electrochem. Soc.* **2001**, *148*, C119−C123.
(25) Bartlett, P. N.; Marwan, J. *Microporous Mesoporous Mater.* **2003**, *62*, 73−79.
(26) El-Safty, S. A.; Hanaoka, T. *Chem. Mater.* **2004**, *16*, 384−400.
(27) Russell, A. E.; Rose, A. *Chem. Rev.* **2004**, *104*, 4613−4635.
(28) Yamauchi, Y.; Momma, T.; Fuziwara, M.; Nair, S. S.; Ohsuna, T.; Terasaki, O.; Osaka, T.; Kuroda, K. *Chem. Mater.* **2005**, *17*, 6342−6348.
(29) Jeng, U.; Su, C. H.; Su, C.-J.; Liao, K.-F.; Chuang, W.-T.; Lai, Y.-H.; Chang, J.-W.; Chen, Y.-J.; et al. *J. Appl. Crystallogr.* **2010**, *43*, 110−121.
(30) Zabinsky, S. I.; Rehr, J. J.; Ankudinov, A.; Albers, R. C.; Eller, M. J. *Phys. Rev. B* **1995**, *52*, 2995−2999.
(31) Attard, G. S.; Leclerc, S. A. A.; Maniguet, S.; Russell, A. E.; Nandhakumar, I.; Bartlett, P. N. *Chem. Mater.* **2001**, *13*, 1444−1446.
(32) Liu, Z.; Ling, X. Y.; Su, X.; Lee, J. Y. *J. Phys. Chem. B* **2004**, *108*, 8234−8240.
(33) Yang, C.-M.; Lin, C.-Y.; Sakamoto, Y.; Huang, W.-C.; Chang, L.-L. *Chem. Commun.* **2008**, *45*, 5969−5971.
(34) Yamauchi, Y.; Ohsuna, T.; Kuroda, K. *Chem. Mater.* **2007**, *19*, 1335−1342.
(35) Hwang, B. J.; Chen, C. H.; Sarma, L. S.; Chen, J. M.; Wang, G. R.; Tang, M.-T.; Liu, D. G.; Lee, J. F. *J. Phys. Chem. B* **2006**, *110*, 6475−6482.
(36) Viswanathan, R.; Hou, G.; Liu, R.; Bare, S. R.; Modica, F.; Mickelson, G.; Segre, C. U.; Leyarovska, N.; Smotkin, E. S. *J. Phys. Chem. B* **2002**, *106*, 3458−3465.
(37) Alayoglu, S.; Zavalij, P.; Eichhorn, B.; Wang, Qi.; Frenkel, A. I.; Chupas, P. *ACS Nano* **2009**, *3*, 3127−3137.
(38) Solomon, E. I.; Hedman, B.; Hodgson, K. O.; Dey, A.; Szilagyi, R. K. *Coord. Chem. Rev.* **2005**, *249*, 97−129.
(39) *Handbook of Chemistry and Physics*, 53rd ed.; CRC Press: Boca Raton, FL, 1972−1973; p D-112.
(40) Jeng, U. S.; Lai, Y. H.; Sheu, H. S.; Lee, J. F.; Sun, Y. S.; Chuang, W. T.; Huang, Y. S.; Liu, D. G. *J. Appl. Crystallogr.* **2007**, *40*, s418−s422.
(41) Brendebach, B.; Bucher, S.; Hormes, J.; Bonnemann, H.; Nagabhushana, K. S.; Brinkmann, R.; Modrow, H. *Phys. Scr.* **2005**, *T115*, 773−775.
(42) Hwang, B.-J.; Sarma, L. S.; Chen, J.-M.; Chen, C.-H.; Shih, S.-C.; Wang, G. R.; Liu, D.-G.; Lee, J.-F.; Tang, M.T. *J. Am. Chem. Soc.* **2005**, *127*, 11140−11145.
(43) Kim, Y.-T.; Lee, H.; Kim, H.-J.; Lim, T.-H. *Chem. Commun.* **2010**, *46*, 2085−2087.
(44) Waychunas, G. A. *Rev. Mineral. Geochem.* **2001**, *44*, 105−166.
(45) Jang, S. G.; Khan, A.; Dimitriou, M. D.; Kim, B. J.; Lynd, N. A.; Kramer, E. J.; Hawker, C. J. *Soft Matter* **2011**, *7*, 6255−6263.